Synthesis of High Ion Conductivity Cubic Garnet $Li_7La_3Zr_2O_{12}$ Solid Electrolyte by Controlling the 8a Oxygen Vacancy

Min Liu, Yuansen Hu, Jianpeng Shi, Yuanpu Cao, and Yu Gong

Abstract We present a novel strategy to synthesize pure cubic garnet $Li_7La_3Zr_2O_{12}$ solid electrolyte at a relatively low temperature (700 °C) by two steps. During the process of obtaining $Li_7La_3Zr_2O_{12}$, the 8a oxygen vacancy in pyrochlore of $La_2Zr_2O_7$ was used to occupy the "Li1" 8a site which the information of tetragonal phase $Li_7La_3Zr_2O_{12}$ requires lithium occupation. The lithium ion conductivity of the obtained cubic garnet $Li_7La_3Zr_2O_{12}$ as high as 1.7×10^{-4} S cm^{-1} at room temperature is consistent with the order of record conductivity in the literatures.

Keywords Cubic garnet · Solid electrolyte · Oxygen vacancy · Ion conductivity

1 Introduction

Solid-state electrolytes play an important role in power batteries that have large electrochemical windows, high energy densities and good electrochemical stabilities [1–4]. Among the oxide solid Li-ionic electrolytes, cubic garnets with nominal composition of $Li_7La_3Zr_2O_{12}$ (LLZO) have been extensively studied as one of the most promising candidate materials having high conductivities ($\sim 10^{-3}$ S cm^{-1}) at ambient temperature. The garnet-type LLZO was first reported by Murugan in 2007 [5]. It has two different crystal structures [6], one cubic termed as $LLZO_c$, and the other tetragonal termed as $LLZO_t$. It has been pointed out that $LLZO_c$ exhibits ionic conductivity two orders of magnitude higher than that of $LLZO_t$. Furthermore, in the process of synthesizing $LLZO_c$, there is always the existence of $LLZO_t$, which limits its application in solid state lithium ion batteries [7]. Therefore, many efforts have been devoted to developing single-phase $LLZO_c$.

Modified synthesis method and supervalent doping were considered as the main manners to stabilize the cubic crystal structure [8–11]. Hang et al. investigated the impact of temperatures on $LLZO_c$ synthesized with traditional solid state method, and found that the sintering temperature determines phase composition, and $LLZO_c$ was

M. Liu (✉) · Y. Hu · J. Shi · Y. Cao · Y. Gong
Department of Technology Centre of Dongfeng Motor Group Co. LTD, Wuhan, China
e-mail: tclium@dfmc.com.cn

China Society of Automative Engineers (eds.), *Proceedings of China SAE Congress 2020: Selected Papers*, Lecture Notes in Electrical Engineering 769,
https://doi.org/10.1007/978-981-16-2090-4_88

obtained when the temperature is above 1150 °C [12]. Subsequently, Rosenkiewitz et al. prepared $LLZO_c$ successfully by wet chemical techniques at 1000 °C [13]. Meanwhile, the supervalent doping was also effective in achieving the $LLZO_C$. Thompson et al. showed the effect of substituting Ta^{5+} for Zr^{4+} on obtaining $LLZO_c$, and demonstrated that 0.25 mol of Li vacancies per formula unit contributes to forming $LLZO_c$ [14]. Previous works have been mostly focused on modifying synthesis method and creating of Li vacancies by supervalent doping. However, these strategies take the way of changing tetragonal to cubic phase, instead of intrinsically avoiding the formation of tetragonal phase.

Herein, we report a novel strategy to directly obtain $LLZO_c$ by controlling the oxygen vacancy at 8a site in pyrochlore $La_2Zr_2O_7$. As is well known, the 8a site in LLZO is an important Li vacancy resulting in the formation of $LLZO_c$. If introduced a positive charge at the 8a position in LLZO, it can effectively prevent the Li ion occupying the 8a position and avoid from forming $LLZO_t$. Using such strategy in this work, we obtained pure $LLZO_c$ successfully. Compared to traditional methods to synthesize $LLZO_c$, our method features pure $LLZO_c$ obtaining by avoiding the generation of $LLZO_t$ and processing at a relatively low temperature. The $LLZO_c$ synthesized using our method demonstrates a decent lithium ionic conductivity of 3.7×10^{-4} S cm^{-1} for grain and 1.7×10^{-4} S cm^{-1} for overall.

2 Experimental Section

Chemicals: $ZrOCl_2 \cdot 8H_2O$, $La(NO_3)_3$, $LiNO_3$ and $NH_3 \cdot H_2O$ were of analytical grade and purchased from Sigma-Aldrich, with 99.9% purity. Deionized water was used in all the experimental process.

Synthesis: Precursor A was prepared from $ZrOCl_2 \cdot 8H_2O$ and $La(NO_3)_3$, with molar ration of La^{3+}:Zr^{4+} = 1:1. First, the two solution were mixed together and stirred for 10 min. Then, the mixture solution was added to dilute ammonia (ammonia: water = 1:2, volume ratio) with a titration rate of one drop per second. Under controlled pH = 10–11 with continuous stirring, a white complex precursor hydroxyl sol was formed, which could be represented as $La(OH)_3 \cdot Zr(OH)_4 \cdot nH_2O$. It was then washed several times by centrifuge under a speed of 3000 r/min to remove Cl^-. After being air-dried at 120 °C, the precursor A became dry powders. Precursor B was synthesized by hand-grinding 1 g of the single-source precursor A and 9 g of nitrate salt (6 g $LiNO_3$ and 3 g $La(NO_3)_3$) with an agate mortar and pestle for a few minutes till fully mixed. The mixture was transferred into a covered nickel crucible and heated to a setting temperature for some time, then cooled to room temperature naturally. The hot ultrapure water was used to wash the product for separation and purification. After drying in an oven at 120 °C for some time, the target nano-powders, $LLZO_c$, were obtained. The illustration of the process and formation mechanism of the $LLZO_c$ was shown in Fig. 1. In order to research their electrical performance, the $LLZO_c$ powders were pressed into pellets by universal testing machine under

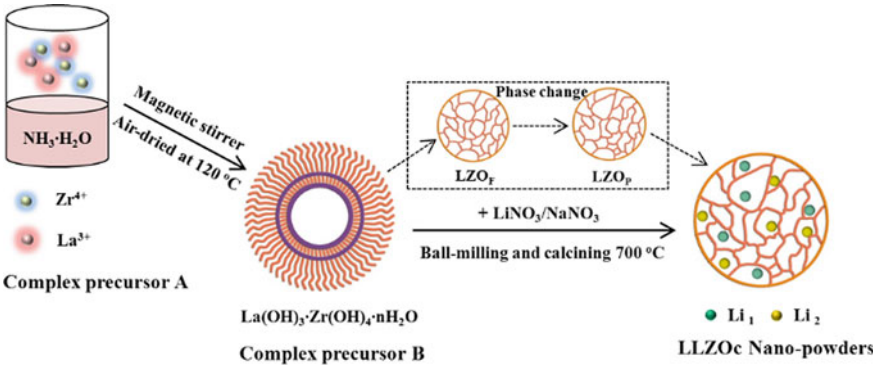

Fig. 1 Illustration of the process and formation mechanism of the $LLZO_c$

200 MPa. The pellets were covered with $LLZO_c$ powders to compensate possible loss of lithium, and finally annealed at 1200 °C for 6 h in an alumina crucible.

Characterization: The crystal structure and phase purity of the samples were examined by means of X-ray Powder Diffraction using Bruker AXS D8-Focus with Ni filtered Cu Kα radiation ($\lambda = 0.154056$ nm). Raman spectra were obtained using Thermo Fisher Scientific Inc 5225 Verona Rd (USA) with a laser wavelength (780 nm) and the spectra were collected in an extended regime in the range of 100–600 cm^{-1}. X-ray photoelectron spectroscopy (XPS) was carried out at bending magnet beamline 9.3.2 at the Advanced Light Source (ALS) in the Lawrence Berkeley National Laboratory (LBNL). XPS data of Li 1s, C 1s, O 1s, Zr 3d and La 4d were collected at 640 eV from the top surface of LLZO samples in ultrahigh vacuum with a sampling size of 1 mm in diameter. Binding energy correction of spectra was done by calibrating to the C 1s photoemission peak of adventitious hydrocarbons at 285 eV. The overview of the morphology and the grain size was checked by Field Emission Scanning Electron Microscope (FESEM; HITACHI SU8010). Electrical conductivity measurements were performed on the prepared circular pellets using Li-ion blocking Au-electrodes (Au pulp covering the pellets was cured at 550 °C for 30 min) over the room temperature using AC impedance spectroscopy (Soartron1287A/1260A, 10 mV; 0.1 Hz–1 MHz).

3 Result and Discussion

According to the strategy of obtaining $LLZO_c$ by use of oxygen vacancy, the pyrochlore $La_2Zr_2O_7$ (LZO_P) was an important intermediate product in this method. In order to characterize the process of phase transformation, XRD and micro-Raman spectroscopic were examined. Figure 2a shows the XRD patterns of the samples prepared at different temperature for 48 h. We found that the LZO_P can be obtained at 600 °C which have two additional characteristic peaks (331) and (511) used to

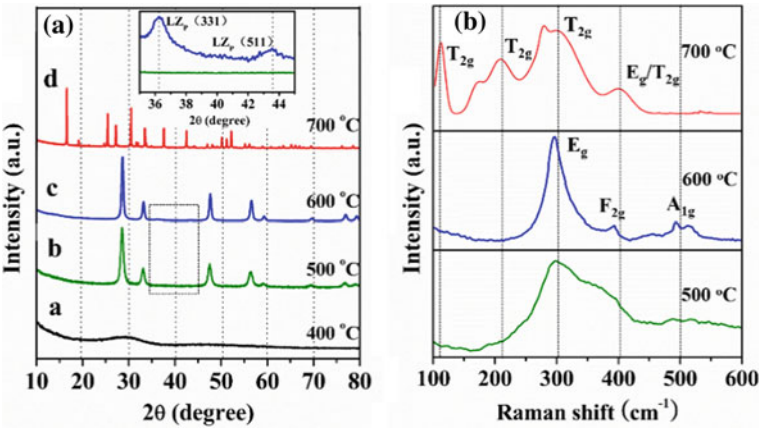

Fig. 2 XRD plots and Raman spectra of samples calcined at different temperature for 48 h

distinguish the defect fluorite from the pyrochlore [15]. When the calcination temperature is lower than 600 °C, only superlattice diffraction peaks of fluorite $La_2Zr_2O_7$ (LZO_F) were observed at 500 °C. While the temperature approaches to 700 °C, we found LZO_P phase disappear, and a new phase of cubic garnet-type LLZO emerged.

3.1 Raman Spectroscopy

Raman spectroscopy is sensitive to metal–oxygen vibrational modes which can be used to distinguish the LZO_F, LZO_P and the phase purity of the $LLZO_c$ [16, 17]. To further confirm the phase structure, Raman was examined in Fig. 2b. It can be observed that there is only one peak E_g at 500 °C which could be described as defect fluorite (LZO_F). From 500 to 600 °C, F_{2g} and A_{1g} were detected and Eg band became sharp. It indicated that the LZO was pure defect fluorite at 500 °C and pure pyrochlore at 600 °C. However, at 700 °C the wavenumbers 107 (T_{2g}), 211 (T_{2g}), 302 (T_{2g}) and 401 (E_g/T_{2g}) appeared, demonstrating the formation of pure cubic garnet structure with I43d space group. Raman spectroscopy results showed that the LZO_F transformed to LZO_P from 500 to 600 °C and to $LLZO_c$ from 600 to 700 °C, which is in good agreement with the XRD results.

3.2 XRD and FESEM Analysis

After sintering at 1200 °C for 6 h for the $LLZO_c$ pellet, XRD and FESEM analysis were performed to characterize the phase stability, and grain size distribution (Fig. 3). From Fig. 3a, it can be seen that the $LLZO_c$ remains cubic garnet structure. Figure 3b

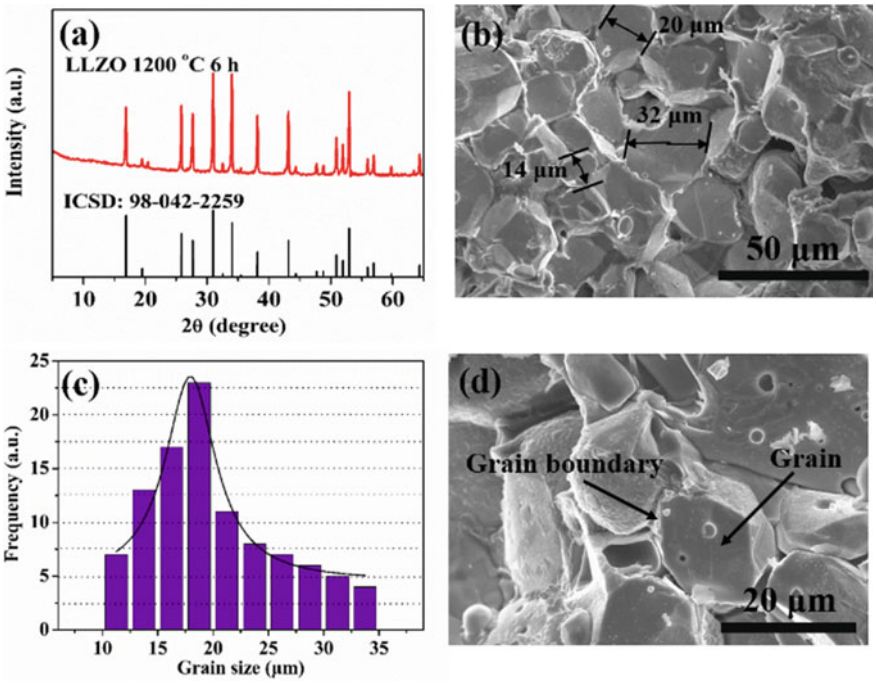

Fig. 3 **a** XRD patterns of $LLZO_c$ pellet calcined at 1200 °C for 6 h, **b** FESEM of fracture surface of calcined $LLZO_c$ pellet, **c** particle size distribution of calcined $LLZO_C$ pellet, **d** a higher magnification micrograph of calcined $LLZO_c$ pellet

showed FESEM image of fracture surface of $LLZO_c$ pellet. In Fig. 3b, we observed the irregular block with the typical grain size distribution of 14–35 μm. At the same time, we recognize relatively low porosity, similar grain sizes were conducive to the conduction of Li ions [18]. The corresponding size distribution of LLZOc was shown in Fig. 3c. The average diameter of $LLZO_c$ grains were approximately 23 μm. Figure 3d showed a higher magnification micrograph of grains and grain boundary. The grain and grain boundary can be clearly distinguished which had a significance to analysis of response to electrical signal for the following AC impedance test [19].

XPS analysis was used to further understand the changes in the oxygen vacancies and binding energy of LZO_P and $LLZO_c$ pellet surface. The spectra of O 1s, Zr 3d, La 4d and Li 1s are shown in Fig. 4. From Fig. 4a, it can be seen that the O 1s have two obvious satellite peaks at 529.1 eV and 53.4 eV of LZO_P which corresponds to two oxygen sites at 48f and 8b, respectively [20]. The change in the O 1s XPS spectra from LZO_P to $LLZO_c$ could be attributed to the structural transform from cubic pyrochlore to cubic garnet. While, it is noted that there is almost no change of Zr 3d and La 4d spectra in Fig. 4b, c. In general, the disorder of oxygen ions or oxygen vacancies will cause the La–O–La and Zr–O–Zr to change [20–22]. This can be explained by the ordered 8a oxygen vacancies of LZO_P which are left in

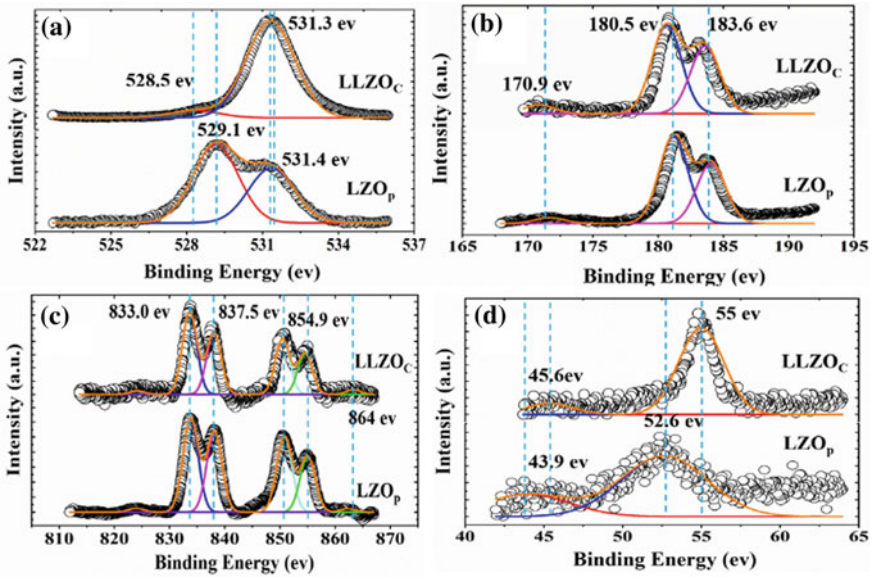

Fig. 4 **a** O 1s, **b** Zr 3d, **c** La 4d and **d** Li 1s XPS data collected from LZO_P and $LLZO_C$ pellet surfaces

the $LLZO_c$ during the transition from LZO_P to $LLZO_c$, just like genetic inheritance. These genetic 8a oxygen vacancies are the key to prevent the formation of $LLZO_t$ and result in the $LLZO_c$ formation. Besides, we further observed weak peak at 52.6 eV of Li 1s for LZO_P in Fig. 4d which demonstrated that a small amount of Li–O bond is present in the LZO_P at 600 °C. After obtaining $LLZO_c$ at 700 °C, Li 1s peak exhibited a sharper peak and shifted to a higher binding energy from 52.6 to 55 eV. It could be a possible reason for forming strong Li–O bond and expansion of cell parameters after Li embedding into the space of LZO_P. Therefore, it can be inferred from the XPS results that $LLZO_c$ inherited the 8a oxygen vacancies in LZO_P, which can prevent the formation of tetragonal phase and directly obtain the cubic phase of LLZO.

3.3 The Formation Process from LZOF Transformed to LLZOc

According to XRD, Raman and XPS results, the schematic of the formation process from LZO_F transformed to $LLZO_c$ can be illustrated in Fig. 5. For $LLZO_t$, there are three different Li sites: "Li1" (8a) site occupied the center of tetrahedral, "Li2" (16f) site and "Li3" (32 g) site occupied the center of two different distorted octahedral [23]. In contrast, there are only two different Li sites in $LLZO_c$: "Li1" (24d) site

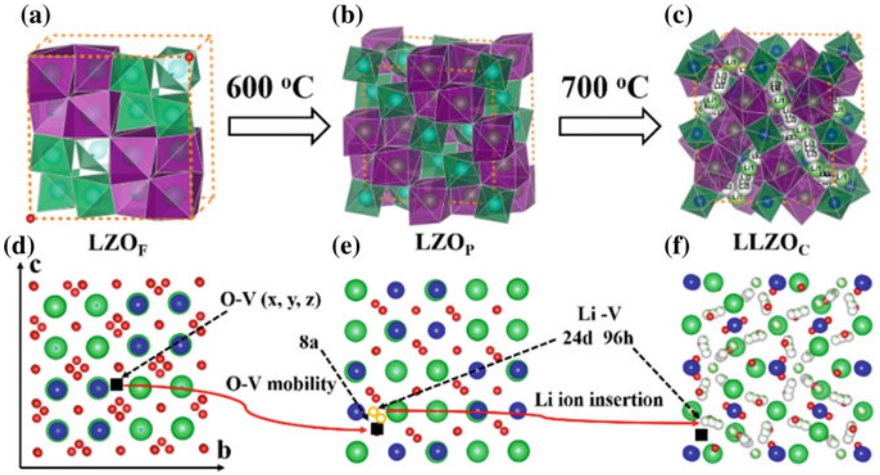

Fig. 5 Schematic of the process formation from LZO_F transformed to $LLZO_C$

occupied the center of tetrahedral and "Li2" (96 h) site occupied the center of distorted octahedral [24]. Therefore, different Li site means different structure and phase of LLZO crystal. In this work, we use oxygen vacancy occupying 8a site to hinder the formation of $LLZO_t$ and contribute to obtain the $LLZO_c$ by use of pyrochlore $La_2Zr_2O_7$ (LZO_P).

As illustrated in Fig. 5, $LLZO_c$ was obtained as follows: (a) the defect fluorite $La_2Zr_2O_7$ (LZO_F) consists of 4 La occupied the 16d site, 4 Zr occupied the 16c site, 14 O occupied the 48f and 8b sites, and disordered oxygen vacancies; (b) after heating at 600 °C, the disordered oxygen vacancies located at 8a and the defect fluorite $La_2Zr_2O_7$ (LZO_F) transformed to LZO_P; (c) when the temperature increases to 700 °C, the introduced Li occupied at 24d and 96 h, leading to and the formaiton of $LLZO_c$. Therefore, we propose that oxygen vacancies are formed in LZO_F first, then disordered and migrated to 8a position, giving rise to LZO_P. At last, the Li embedded into the space outside the 8a position, enabling the formation of $LLZO_c$. The process of forming $LLZO_c$ is shown in Fig. 5d–f.

3.4 AC Impedance Spectroscopy Analysis

The ionic conductivity of $LLZO_c$ at ambient temperature was determined by AC impedance spectroscopy of sintered pellet with attached symmetrical Au electrodes. A typical Nyquist plot of the $LLZO_c$ pellet measured at ambient temperature was displayed in Fig. 6a. The impedance data were fitted with an equivalent circuit shown in the inset of Fig. 6a. The grains resistance and grain boundary resistance are represented as Rg and Rgb in the equivalent circuit. Constant phase elements (CPE) were

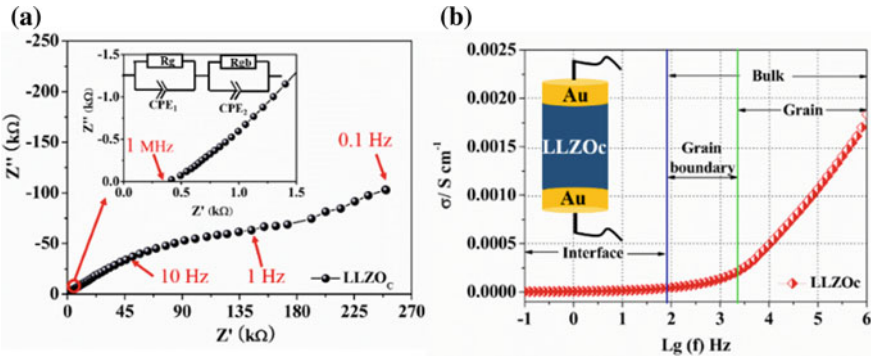

Fig. 6 **a** Nyquist plot of a $LLZO_c$ pellet with Au electrodes measured at room temperature. **b** Arrhenius plot for frequency of the bulk ionic conductivity of $LLZO_c$. (Inset) Measurement schematic displaying $LLZO_c$ pellet

used to fit [25]. The formula $\sigma = d/(A \cdot R)$ was used to calculate the lithium ionic conductivity σ. Where d is the thickness of pellet, A is the area of Au electrodes and R is the value of fitted resistance by CPE [4]. The measurements showed an offset of the impedance response at high frequencies, a semicircle for intermediate frequencies, and a tail for low frequencies. We attribute these to grain resistance, grain boundary resistance, and double layer capacitance due to ion blocking by electrodes, respectively [26]. Arrhenius plot for frequency of the bulk ionic conductivity of $LLZO_c$ is shown in Fig. 6b. Notably, a high ionic conductivity of 3.7×10^{-4} S cm^{-1} for grain and 1.7×10^{-4} S cm^{-1} for overall, which is in good agreement with the literature [8, 10]. Compared with the modified synthesis method and supervalent doping method, the control of oxygen vacancy is a novel strategy to obtain pure $LLZO_c$ with high ionic conductivity.

4 Conclusion

In summary, we prepared pure $LLZO_c$ by utilize of oxygen vacancy of LZO_P at 700 °C for the first time. In this process, we used oxygen vacancy occupied 8a site use of LZO_P which formed $LLZO_t$ of L1 site, and then the introduced Li occupied 24d and 96 h site and formed $LLZO_c$. Through this novel strategy, we can directly obtain pure phase $LLZO_c$ at lower temperature (700 °C), rather than the $LLZO_t$ by the traditional method. When the $LLZO_c$ was used as solid Li-ionic solid electrolytes, it exhibited a high conductivity of 1.7×10^{-4} S cm^{-1}. In a word, this method provided a new idea for the synthesis of solid electrolyte materials with high ionic mobility.

Acknowledgements This work was financially supported in part by Department of Technology center of Dongfeng motor group Co. LTD (91224Y180014) and 928 project of Dongfeng motor group Co. LTD (912249282014).

References

1. Broek J, Af Yon S, Rupp J et al (2016) Interface-engineered all-solid-state li-ion batteries based on garnet-type fast li+ conductors. Adv Energy Mater 6(19):1600736
2. Yu S, Schmidt RD, Garciamendez R et al (2016) Elastic Properties of the Solid Electrolyte $Li_7La_3Zr_2O_{12}$ (LLZO). Chem Mater 28(1):197–206
3. Zhang J, Zhao N, Zhang M et al (2016) Flexible and ion-conducting membrane electrolytes for solid-state lithium batteries: Dispersion of garnet nanoparticles in insulating polyethylene oxide[J]. Nano Energy 28(28):447–454
4. Zhang Q, Schmidt N, Lan J et al (2012) A facile method for the synthesis of the $Li_{0.3}La_{0.57}TiO_3$ solid state electrolyte. Chem Commun 50(42):5593–5596
5. Murugan R, Thangadurai V, Weppner W et al (2007) Fast Lithium Ion Conduction in Garnet-Type $Li_7La_3Zr_2O_{12}$. Angew Chem 46(41):7778–7781
6. Liu C, Rui K, Shen C et al (2015) Reversible ion exchange and structural stability of garnet-type Nb-doped $Li_7La_3Zr_2O_{12}$ in water for applications in lithium batteries. J Power Sources 282:286–293
7. Han J, Zhu J, Li Y et al (2012) Experimental visualization of lithium conduction pathways in garnet-type $Li_7La_3Zr_2O_{12}$. Chem Commun 48(79):9840–9842
8. Thangadurai V, Narayanan S, Pinzaru D et al (2014) Garnet-type solid-state fast Li ion conductors for Li batteries: critical review. Chem Soc Rev 43(13):4714–4727
9. Quinzeni I, Capsoni D, Berbenni V et al (2017) Stability of low-temperature $Li_7La_3Zr_2O_{12}$ cubic phase: the role of temperature and atmosphere. Mater Chem Phys 55–64
10. Wagner R, Redhammer GJ, Rettenwander D et al (2016) Fast li-ion-conducting garnet-related $Li_7–3xFexLa_3Zr_2O_{12}$ with Uncommon $I\bar{4}3d$ Structure. Chem Mater 28(16):5943–5951
11. Mukhopadhyay S, Thompson T, Sakamoto J et al (2015) Structure and stoichiometry in supervalent doped $Li_7La_3Zr_2O$. Chem Mater 27(10):3658–3665
12. Huang M, Liu T, Deng Y et al (2011) Effect of sintering temperature on structure and ionic conductivity of $Li_{7-x}La_3Zr_2O_{12-0.5x}$ ($x = 0.5 \sim 0.7$) ceramics. Solid State Ionics 204:41–45
13. Rosenkiewitz N, Schuhmacher JD, Bockmeyer M et al (2015) Nitrogen-free sol-gel synthesis of Al-substituted cubic garnet $Li_7La_3Zr_2O_{12}$ (LLZO). J Power Sources 278(278):104–108
14. Thompson T, Wolfenstine J, Allen JL et al (2014) Tetragonal vs. cubic phase stability in Al-free Ta doped $Li_7La_3Zr_2O_{12}$ (LLZO). J Mater Chem 2(33):13431–13436
15. Wang Y, Yang F, Xiao P et al (2014) Role and determining factor of substitutional defects on thermal conductivity: a study of La2(Zr1-xBx)2O7 ($B = Hf, Ce, 0 \leqslant x \leqslant 0.5$) pyrochlore solid solutions. Acta Materialia 68:106–115
16. Orera A, Larraz G, Rodriguezvelamazan JA et al (2016) Influence of Li+ and H+ distribution on the crystal structure of Li7-xHxLa3Zr2O12 ($0 \leq x \leq 5$) Garnets. Inorg Chem 55(3):1324–1332
17. Ou G, Liu W, Yao L et al (2014) High conductivity of La2Zr2O7 nanofibers by phase control. J Mater Chem 2(6):1855–1861
18. Ilina EA, Andreev OL, Antonov BD et al (2012) Morphology and transport properties of the solid electrolyte $Li_7La_3Zr_2O_{12}$ prepared by the solid-state and citrate-nitrate methods. J Power Sources 201:169–173
19. Huggins RA (2002) Simple method to determine electronic and ionic components of the conductivity in mixed conductors a review. Ionics 8(3):300–313
20. Pokhrel M, Wahid K, Mao Y et al (2016) Systematic Studies on RE2Hf2O7:5%Eu3+ (RE = Y, La, Pr, Gd, Er, and Lu) nanoparticles: effects of the A-Site RE3+ cation and calcination on structure and photoluminescence. J Phys Chem C 120(27):14828–14839
21. Cheng L, Crumlin EJ, Chen W et al (2014) The origin of high electrolyte-electrode interfacial resistances in lithium cells containing garnet type solid electrolytes. Phys Chem Chem Phys 16(34):18294–18300
22. Cheng L, Wu CH, Jarry A et al (2015) Interrelationships among Grain Size, Surface Composition, Air Stability, and Interfacial Resistance of Al-Substituted $Li_7La_3Zr_2O_{12}$ solid electrolytes. ACS Appl Mater Interfaces 7(32):17649–17655

23. Meier K, Laino T, Curioni A et al (2014) Solid-state electrolytes: revealing the mechanisms of li-ion conduction in tetragonal and cubic LLZO by first-principles calculations. J Phys Chem C 118(13):6668–6679
24. Yi E, Wang W, Kieffer J et al (2016) Flame made nanoparticles permit processing of dense, flexible, Li+ conducting ceramic electrolyte thin films of cubic-$Li_7La_3Zr_2O_{12}$ (c-LLZO). J Mater Chem 4(33):12947–12954
25. Rettenwander D, Welzl A, Pristat S et al (2016) A microcontact impedance study on NASICON-type Li1+xAlxTi2-x(PO4)3 ($0 \leq x \leq 0.5$) single crystals. J Mater Chem 4(4):1506–1513
26. Tenhaeff WE, Rangasamy E, Wang Y et al (2014) Resolving the grain boundary and lattice impedance of hot-pressed $Li_7La_3Zr_2O_{12}$ garnet electrolytes. ChemElectroChem 1(2):375–378